Dynamic Rail Near-surface Inspection of Multi-physical Coupled Electromagnetic and Thermography Sensing System

Haoran Li, Bin Gao, *Senior Member*, *IEEE*, Xiaolong Lu, Xiyuan Zhang, Yunhan Shi, Gaige Ru, Wai Lok Woo, *Senior Member*, *IEEE*

***Abstract*—The effectiveness of railway fault inspection has remained challenging. Conventional techniques are still functionally limited and unable to meet the increasing demand of railway diagnosis. To mitigate the variety of rail fault detection problems, this paper proposes a dynamic railway inspection system based on multi-physical coupled electromagnetic and thermography sensing. It further shows the development and construction of a new inverted L-type magnet yoke abreast with volumetric coils array. The novel structure can not only significantly enhance the sensitivity and detectability of the region of interest (ROI), but also effectively detect the subsurface defects with the compensation of coils array due to the coupled electromagnetic field. Furthermore, the theoretical analysis of the coupled physical fields has been derived and proved to be consistent with the numerical simulation results. A rail test sample with various defects is carried out to verify the feasibility of the proposed system. Additionally, a metric learning post-processing algorithm has been conducted for distilling eddy current signals and thermograms to improve the accuracy of the detection results. On-site experimental and contrast results with various levels of performance validation have demonstrated that the integrated system is well suited for dynamic rail inspection on near-surface cracks at speed of 1 km/h.**

***Index Terms*—Railway fault diagnosis, dynamic defect detection, multi-physical coupled sensing, anomaly detection.**

I. Introduction

The rapid development of the world's high-speed railway network creates new challenges for its maintenance and security assurance. As a class of serviceable approaches, railway fault diagnosis and monitoring technologies have received more attention to their roles in ensuring the long-term safety operation of such infrastructures and it has become an indispensable tache to make many irreplaceable contributions for avoiding considerable losses in the event of natural or man-made disasters in railway system [1][2].

At present, there are five mainstream non-destructive testing (NDT) methods for railway defects inspection, including magnetic flux leakage testing (MFL), ultrasonic testing (UT), acoustic emission testing (AET), visual testing (VT) as well as eddy current testing (ET). MFL is suitable for detecting the discontinuity of the near-surface of rails and has ultra-high sensitivity with the aid of certain high-performance magnetic sensors [3][4][5]. Regrettably, it requires rich testing experience of inspectors and has a low spatial resolution for visualization. UT is good at evaluating deep defects in rail web and has a high degree of automation, however, it is not easy to inspect specimens with complex geometry shapes and is inseparable from various couplants [6][7]. AET provides an opportunity for real-time online monitoring of rail cracks propagation, worryingly, it has extremely high requirements of signal noise suppression [8][9]. VT has the advantages of simple operation, low cost, intuitive display, and superhigh resolution for opening cracks, whereas the fault inspection relies on a clean background which is easily broken by the heterogeneous geometric structure of rails [10][11]. ET plays a high-efficient role in near-surface defects detection in metal materials field and it is competent in long-distance rail inspections due to its low energy consumption and high sensitivity. Nevertheless, the results are tough to quantify and susceptible to lift-off effects [12][13].

As a gradually maturing near-surface fault diagnosis technique, eddy current thermography (ECT) is rapidly being adopted in many engineering fields, including railway inspection [14][15]. It is a multi-physical coupling method that combines three physical effects of electricity, magnetism and heat. The enormous advantages of ECT include high spatial resolution and sensitivity, in which, the two-dimensional sequences are intuitive and tractable. Moreover, ECT has made some new advances in irregular geometry workpieces detection and proves that it has the potential for rail inspection. Unfortunately, the uneven surface emissivity and weak penetrability, especially in ferromagnetic materials, limit its application in certain occasions. It is worth noting that even as homogenous detection techniques (the similar excitation principles of electromagnetic induction), few researches have focused on fusing ET and ECT to complement their advantages for more much-needed application scenarios.

To surmount the above challenges, several studies have been carried out. Wang *et al*. [16] analyzed the magnetization intensity and permeability of ferromagnetic materials along with the duration of dynamic magnetization process and verified that the MFL technique could achieve effective defect inspection at high speeds with the maximum inspection speed of about 200 km/h. Hu *et al*. [17] proposed a new method for the in-situ and rapid detection of cracks in the rail foot by ultrasonic B-scan imaging which could increase the lift-off, eliminate the noise and improve the detection efficiency. Thakkar *et al*. [18] presented a laboratory study on the acoustic emission generated during railway wheel-rail track interaction, with a view to developing methods of in situ rail-wheel interaction monitoring using rail-mounted sensors. Resendiz *et al*. [10] developed a computer vision system consisting of field-acquired video as well as subsequent analysis, and it could improve the detection efficiency compared to the previous methods. Song. [19] evaluated two different types of artificial defects in a railhead to analyze the relationship between different types of defects and eddy current signals, then succeed in obtaining data on the size of the rail surface defects and crack location. Li *et al*. [20] built a multiphysics structured system for dynamic detection of both artificial and natural cracks while it has

not yet carried out mechanism insight studies. Gao *et al.* [21] combined magnetic flux leakage (MFL) and eddy current pulsed thermography (ECPT) of a new sensing structure to enhance the detection performance for multiple cracks evaluation. However, most of these researches were aimed at overcoming certain shortcomings of a single technology or still retaining the specific limitation by using multiphysics linked methods, which renders it difficult to satisfy the serious demands of dense railway network inspection. Thus, it becomes particularly urgent to establish an efficient and accurate system for rail detection.

In this paper, a dynamic detection system for rail inspection based on the multi-physical coupling structure of electromagnetic and thermography sensing is proposed. The contributions are listed below:

1) The physical combination of ET and ECT techniques is made possible by the innovative construction of inverted L-type magnet yoke will significantly enhance the sensitivity and detectability of ROI due to its abilities of gathering magnetic flux, reducing the leakage while making the electromagnetic field between its two arms (ROI) obtain relative uniform. It is proven to be effective in the application of rail near-surface defect diagnosis.

2) The proposed integrated prototype is more effective for detecting the buried defects with the compensation of four volumetric coils array abreast with the magnet yoke which means an expansion of the categories of detectable defects. And it is also competent for detecting the rail cracks of multiple categories in the dynamic case and has the ability to automatically identify defects with the aid of the abnormal learning strategy. It further lays the foundation for long-distance automated railway safety inspections which is urgently required in the field of railway diagnosis industrial application.

II. METHODOLOGY

A. Configuration of the Dynamic Detection System

The schematic diagram of dynamic detection system for rail is shown in Fig. 1. High-frequency power currents are perceived as the excitation signal which is generated by an excitation source for dozens of seconds. It drives the sensing structure and produces a strong alternating electromagnetic field which could induce eddy currents on the near-surface of the rail. When it works, the carrier moves along the rail at a certain speed and a synchronous controller will dominate the working sequence of the IR camera as well as excitation source to ensure that the whole thermal information during this period is recorded by the IR camera. Meanwhile, the electromagnetic signals will be acquired by the data acquisition (DAQ) card and transmitted to a PC for post-processing.

In particular, the drawing of this novel sensing structure is shown in Fig. 2. It can be seen that the coils array is fixed beside one of the yoke arms by 3D print and PCB holders which are just fit to the geometry of the yoke. The reasons for adopting the inverted L-type magnet yoke are that this structure can not only gather the magnetic flux to enhance the detection sensitivity but also release the observation area (ROI). Thus, the IR camera can conveniently capture thermal information from a vertical viewing angle to reduce the effect of low or uneven surface radiation intensity. The arrangement of four volumetric coils is to cover most of the

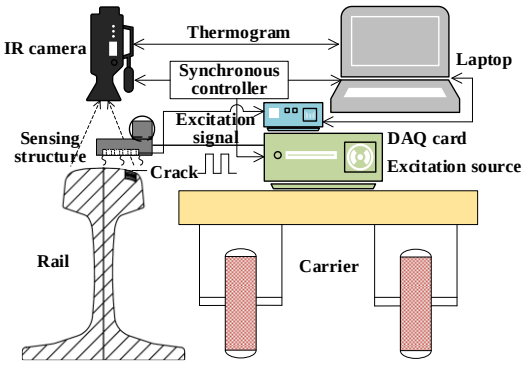

Fig. 1 Schematic diagram of the dynamic detection system.

detection areas which are corresponding to ROI, it can supplement the defects information on the subsurface of the rail which is a serious challenge for electromagnetic infrared thermography technology. Thus, instead of simply adding the two technologies together, the detection process of the ET and ECT is not separate. The electromagnetic and thermal fields are generated simultaneously and uniformly by one excitation.

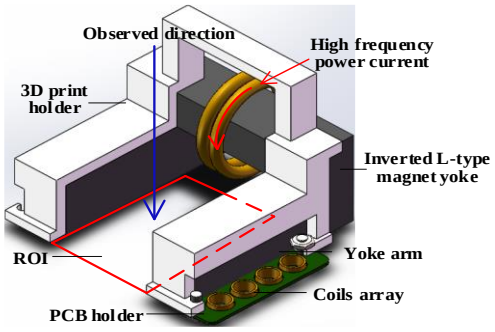

Fig. 2 Sensing structure.

B. Mathematical Models of the Coupling Field

According to the law of electromagnetic induction, an excitation coil with alternating currents will generate an alternating magnetic field (primary field). When it gets close to a conductor, eddy currents can be induced and they will generate a new magnetic field (secondary field), which is going to be superimposed on the primary one. Based on differential Maxwell's equations, superimposed magnetic fields should satisfy:

$$\nabla \times \frac{1}{\mu}\left(\nabla \times \vec{A}\right) = \vec{J_s} - \sigma\frac{\partial \vec{A}}{\partial t} + \frac{\partial \vec{D}}{\partial t} \tag{1}$$

$$\nabla \times \vec{E} = -\frac{\partial \vec{B}}{\partial t} \tag{2}$$

where $\vec{A}$ indicates the magnetic vector potential, μ is the magnetic permeability, $\vec{J_s}$ is the conduction-current density, $\vec{D}$ is the electric displacement vector, and $\vec{E}$ is the electric field intensity. Furthermore, $\vec{B}$ is the magnetic flux density which can be defined as:

$$\vec{B} = \nabla \times \vec{A} \tag{3}$$

In the light of Lorentz force, motional current will be generated while there is relative motion between the sensing structure and rail. The density of this motional current could be expressed as:

$$\vec{J_v} = \sigma\vec{v} \times \vec{B} \tag{4}$$

where σ is the electrical conductivity of the rail and $\vec{v}$ represents the relative velocity.

Therefore, when speed-effect is taken into consideration,

the motional current should be added to (1), and the superimposed field governing equation employed in this study should be rewritten as:

$$\nabla \times \frac{1}{\mu}\left(\nabla \times \vec{A}\right) = \vec{J_s} - \sigma\frac{\partial \vec{A}}{\partial t} + \sigma\vec{v} \times \vec{B} + \frac{\partial \vec{D}}{\partial t} \tag{5}$$

where $-\sigma\frac{\partial \vec{A}}{\partial t}$ denotes the induced eddy current density and $\sigma\vec{v} \times \vec{B}$ denotes the motional current density. It should be noted that the impact of the electric displacement vector could be neglected while the operating frequency is lower than 10 MHz. Therefore, it is feasible to detect the defects by monitoring the changes of the magnetic field on account of the differentiation of the characteristic parameters between specimen and air.

In addition, performing convolution operation on both ends of (2), with the addition of constitutive relation [22]:

$$\frac{1}{\sigma}\nabla \times \nabla \times \vec{J} = -\mu\frac{\partial \vec{J}}{\partial t} \tag{6}$$

Simplifying (6), it becomes:

$$\frac{\partial \vec{J}}{\partial t} = \frac{1}{\sigma\mu}\nabla^2\vec{J} \tag{7}$$

where $\vec{J}$ expresses the superimposed current density of induced eddy current and motional current. (7) illustrates that while the relative speed, excitation frequency, current magnitude and lift-off, etc. remain constant, the diffusion rate of superimposed current is affected by σ and μ. Namely, the existence of defects will break the stability of the inspection process and cause signal fluctuations. Eqns. (1)-(7) derive the governing equation of electromagnetic field in dynamic case, they contain information of electric and magnetic fields, which are important to analyze the factors affecting the acquisition of coils array in the sensing structure.

In terms of magnetic flows, while the proposed structure is positioned over a specimen, as shown in Fig. 3, the equivalent magnetic flows stimulated by the inverted L-type magnet yoke could be divided into 3 paths. Path_1 represents the leakage fluxes which are not imported into the magnet yoke and assuming the average length of them is $l_{leakage}$. Path_2 represents the fluxes passing though part of the two magnet yoke arms besides the air between them, the average lengths in the yoke and air could be assumed as l_x and l_{air}, respectively. Path_3 represents the fluxes passing though part of the two magnet yoke arms, the gap between arms and rail surface, as well as the specimen of rail under the yoke. The lengths of path_3 could be assumed as the sum of l_x, l_{gap} and $l_{specimen}$. The equivalent magnetic circuit of the model is shown in Fig. 4. According to the determinant of the magnetic resistance and above analysis, the magnetic resistances in Path_1, Path_2, Path_3 can be severally expressed as:

$$R_{m1} = R_{mair1} = \frac{l_{leak}}{\mu_0 A_{air1}} \tag{8}$$

$$R_{m2} = R_{mx} + R_{mair2} = \frac{l_x}{\mu_{yoke}A_{yoke}} + \frac{l_{air}}{\mu_0 A_{air2}} \tag{9}$$

$$R_{m3} = R_{mx} + R_{mgap} + R_{mspecimen} = \frac{l_x}{\mu_{yoke}A_{yoke}} + \frac{l_{gap}}{\mu_0 A_{gap}} + \frac{l_{specimen}}{\mu_{specimen}A_{specimen}} \tag{10}$$

where R_{m1}, R_{m2}, R_{m3} are the magnetic resistances in path_1, path_2, path_3, respectively. R_{mair1}, R_{mair2}, R_{mgap}, $R_{mspecimen}$ are the magnetic resistances in the air, gap and specimen. R_{mx} represents the resistance in the path_2 or path_3 in part of the yoke, the length is x. μ_0, μ_{yoke} and $\mu_{specimen}$ denote the magnetic permeability of the air, yoke and specimen. A_{air1}, A_{air2}, A_{yoke}, A_{gap} and $A_{specimen}$ denote the effective areas of air, yoke, gap and specimen, respectively.

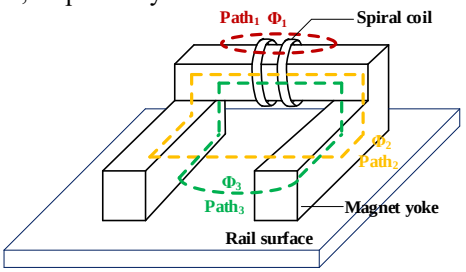

Fig. 3 Flux paths of the magnet yoke.

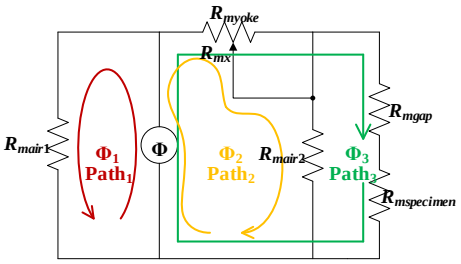

Fig. 4 Equivalent magnetic circuit.

Similar to the currents, fluxes always tend to flow along with low magnetic resistance loops. Due to the ferromagnetic properties of the rail specimen, the relationship among μ_0, μ_{yoke} and $\mu_{specimen}$ in this model can be expressed as $\mu_{yoke} \gg \mu_{specimen} \gg \mu_0$. Thus, when the lift-off distance l_{gap} is much less than that between the two yoke arms, it will be more beneficial to guide the fluxes into the specimen. However, excessive distance between the two arms will lead to higher flux loss due to the increase of the magnetic resistances. In addition, to obtain the maximum radiation intensity of rail surface, IR camera also needs a wide enough field of perpendicular view to observe the ROI. According to Lambert's cosine law (as shown in Fig. 5), the observed direction of IR camera should be perpendicular to the plane source:

$$I_\theta = I_0\cos\theta \tag{11}$$

where I_0 denotes radiation intensity in the normal direction of the surface, θ denotes the angle between the observed direction and surface normal. It indicates that the radiation intensity is the strongest in the normal direction of the surface. Therefore, the viewing angle of the IR camera should be selected to the normal direction of the surface.

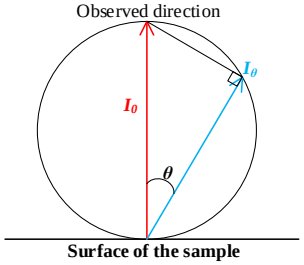

Fig. 5 The radiant intensity depends on the direction of emission.

In terms of coupling field, as known from Joule's law, heat is produced while currents flow through a conductor, and they will be restricted to the near-surface due to the skin effect. This phenomenon can be described as:

$$\delta = \frac{1}{\sqrt{\pi\sigma\mu f}} \tag{12}$$

where δ is the skin depth, f is the induction frequency which is equal to the excitation current frequency. It can be seen that the skin depth is related to the induction frequency, conductivity and permeability of the tested materials. As a heat source, the heating power generated by the current can be expressed as:

$$Q = \frac{1}{\sigma}\left|\vec{J}_e + \vec{J}_v\right|^2 \tag{13}$$

where Q represents the strength of the heat source, $\vec{J}_e = \sigma\vec{E}$ denotes the density of eddy current, $\vec{J_v}$ denotes the density of motional current. In ferromagnetic materials like rails, the heat generated by induced currents is concentrated on the surface and this can be regarded as a line or plane heat source due to the high magnetic permeability and electrical conductivity of these materials.

Assuming that the distributions of the electric field and magnetic field between the two arms of the inverted L-typed magnet yoke are uniform, as analyzed above, the heat generated by induced currents can be considered as a uniform plane heat source. As shown in Fig. 6, the red box area which is located directly below the sensing structure indicates the plane heat source generated by superimposed currents. It can be divided into numbers of line sources and define the *i*-th one as dx_i. Thus, under the influence of this infinitesimal strip heat source, the temperature rise expression at point *M* is:

$$d_{\theta M} = \frac{Q_m dx_i}{2c\rho(4\pi a\tau)} \cdot e^{-\frac{z^2+(x-x_i)^2}{4a\tau}} \cdot \left[\mathrm{erf}\left(\frac{y}{\sqrt{4a\tau}}\right) - \mathrm{erf}\left(\frac{y-L}{\sqrt{4a\tau}}\right)\right] \tag{14}$$

The total temperature rise caused by the entire plane heat source to point *M* is:

$$\theta_M = \frac{Q_m}{2c\rho(4\pi a\tau)} \cdot \left[\mathrm{erf}\left(\frac{y}{\sqrt{4a\tau}}\right) - \mathrm{erf}\left(\frac{y-L}{\sqrt{4a\tau}}\right)\right] \cdot e^{-\frac{z^2}{4a\tau}} \int_0^B e^{-\frac{x-x_i}{4a\tau}} dx_i \tag{15}$$

where θ_M indicates the temperature rise at point *M*(*x*,*y*,*z*), Q_m denotes the instantaneous calorific value of plane source, c and ρ denote the specific heat capacity and density of the rail respectively, a denotes the thermal diffusivity and τ is the duration time. Moreover, x_i represents the distance between infinitesimal strip source and original point *O*, *B* and *L* are the length and width of the plane heat source respectively.

Eqn. (15) can be solved as [23]:

$$\theta_M = \frac{Q_m}{4c\rho(4\pi a\tau)^{\frac{1}{2}}} \cdot e^{-\frac{z^2}{4a\tau}} \cdot \left[\mathrm{erf}\left(\frac{y}{\sqrt{4a\tau}}\right) - \mathrm{erf}\left(\frac{y-L}{\sqrt{4a\tau}}\right)\right] \cdot \left[\mathrm{erf}\left(\frac{x}{\sqrt{4a\tau}}\right) - \mathrm{erf}\left(\frac{x-B}{\sqrt{4a\tau}}\right)\right] \tag{16}$$

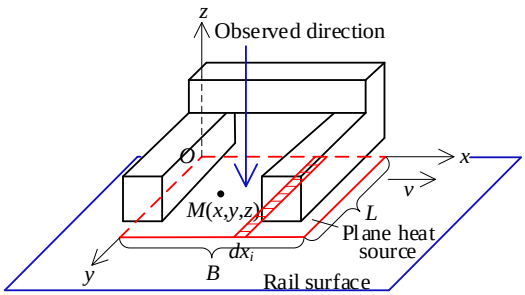

Fig. 6 Temperature field coordinates of plane heat source.

The sensing structure will move along the positive direction of *x*-axis at the speed of v. Hence, the heat source duration time τ could be considered as B/v and the total calorific value of plane source during this time is given as:

$$Q_m = Q\tau = Q\frac{B}{v} \tag{17}$$

Furthermore, in the process of inspection, only the temperature rises on the rail surface (the *x*-*O*-*y* plane) is concerned. Then the coordinates of point *M*(*x*,*y*,*z*) should be updated to *M*(*x*,*y*,0), and θ_M in a semi-infinite medium model ought to be twice that of in the infinite one due to the law of energy conservation as well as adiabatic boundary conditions. In conclusion, taking all the above prerequisites into consideration, during this relatively short period of time, (12) can be rewritten as:

$$\theta_M = \frac{Q\sqrt{v}}{4c\rho\sqrt{\pi aB}} \cdot \left[\mathrm{erf}\left(\frac{y}{\sqrt{4a\frac{B}{v}}}\right) - \mathrm{erf}\left(\frac{y-L}{\sqrt{4a\frac{B}{v}}}\right)\right] \cdot \left[\mathrm{erf}\left(\frac{x}{\sqrt{4a\frac{B}{v}}}\right) - \mathrm{erf}\left(\frac{x-B}{\sqrt{4a\frac{B}{v}}}\right)\right] \tag{18}$$

When there exist defects in the inspected area, the electric and magnetic fields between yoke arms are disturbed and eddy currents will flow around the defects, this results in uneven distribution of heat and a large amount of heat will be accumulated at the tips or edges of the defects. In this way, the defects can be effectively distinguished by monitoring the temperature variation of the rail surface and the signal fluctuations of the coils array. It is noteworthy that during the moving excitation process, although the heat will diffuse to the front and rear areas of the plane source, the effects can be responsibly ignored when the scan velocity of the excitation source is greater than 0.5 cm/s in the steel material specimens [23].

It should be noted that Eqn. (18) is which enoughly take account of the physical dimensions (the distance between the yoke arms *B* and the length of the arm *L*) as well as the inspection speed *v* of the innovative inverted L-type magnet yoke. In particular, assuming point *M* is located at the center and surface (*x*=*B*/2, *y*=*L*/2, *z*=0) of the plane heat source, meanwhile, plugged the whole known parameters into Eqn. (18), the temperature rise θ_M at point *M* can be calculated as about 0.4℃, which is roughly consistent with the simulation or experimental values while there is no defect on the near-surface of the specimen. However, the analytical model will become exceptionally complex when defects are taken into consideration, hence, it is necessary to incorporate numerical simulations verification to ensure the feasibility and effectiveness of the proposed sensing structure.

C. *Physically Linked Abnormal Learning Strategy*

In order to establish the correlations between defect diagnosis and available physical quantities more intuitively, the abnormal score is computed by combining ET and ECT signals:

$$S = f\left(S_t(\theta), S_c(A,k)\right) \tag{19}$$

$$f\left(S_t(\theta), S_c(A,k)\right) = w_1 \times S_t(\theta) + w_2 \times S_c(A,k) \tag{20}$$

where S indicates the abnormal score, $f(\cdot)$ represents the decision function which denotes the weighted sum of anomaly scores, w_1 and w_2 are hyper-parameters which could balance the importance of thermal and voltage signals. In addition, $S_t(\theta)$ and $S_c(A,k)$ are the abnormal detection models based on thermal and voltage signals, respectively. θ is the temperature rise which can reflect the abnormal area in thermograms. A and k indicate the relative amplitude and slope which are associated with crack depth, burial depth and length in coil voltage signals. One-class support vector machine (OC-SVM) [24] is applied to detect time series abnormal patterns in coil voltage signals, which can be defined as $S_c(A,k)$:

$$S_c(A,k) = \left(\sum_{i=1}^{n} d_i \cdot K(e_i, A, k) - b\right)^2 \tag{21}$$

where d_i, e_i, and b are coefficients, kernel vectors, and threshold learned by OC-SVM, respectively. An anomaly detection model [25] is developed to detect the abnormal patterns, which can be defined as $S_t(\theta)$.The main process are shown in Fig. 7. In this model, the auto-encoder trained with normal samples is applied to extract the feature maps which is 1/8 of the original image in size ($W/8 \times H/8 \times C$). The feature maps are then expanded as $W/8 \times H/8$ feature vectors as anomaly scores are computed according to these vectors. For each feature vector q_i, the memory item m_i closest to the feature vector is selected as the matched memory item according to Euclidean distance. In particular, the distance between the feature vector and corresponding memory item is considered as the anomaly score. Once the feature vector is corresponding to one kind of background pattern, there exists a matched memory item close to it, and vice versa. Thus, the distance (L2) represents the matching degree between the feature vector and background pattern. Finally, all the anomaly scores are reconstructed as the anomaly map according to the position of the corresponding feature vectors, while the max value in the anomaly score map can be applied as the image-level anomaly score ($S_t(\theta)$). It should be noted that the image region corresponding to the feature vector is defined as patch p_i.

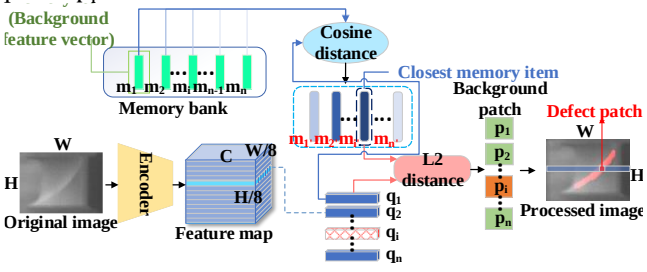

Fig. 7 Framework of the anomaly detection method.

III. Simulation And Experiment Set-up

A. *Numerical Simulations and Analysis*

Numerical simulation is one of the most effective ways to verify the feasibility and effectiveness of the proposed system. For the sake of compensating the deficiency of analytical calculation and exploring the mechanism of this electromagnetic and thermal sensing structure in dynamic case, several finite element simulation models based on COMSOL Multiphysics 5.6 for dynamic rail inspection contains the inverted L-type magnet yoke as well as rail specimen with several cracks are constructed.

Fig. 8 shows the space diagram of the finite element model. The basic components of this model are spiral coil, magnet yoke and rail piece, which are made of copper, ferrite core as well as ferromagnetism steel, and their relevant physical parameters are listed in Table I. In geometric dimensioning, the length, width and height of the rail are 300 mm, 200 mm and 250 mm, respectively. The major and minor radius of the spiral coil with double turns are 14 mm and 3 mm, and the inverted L-type magnet yoke is spliced by three 50 mm×15 mm×10 mm cuboids, which are consistent with the on-site experimental system. The specific dimensions are shown in Fig. 9 and the distance between the two arms is set to 30 mm, which is far greater than the lift-off distance l_{gap} (5 mm). In addition, six cracks with varying tread lengths are fabricated on the surface of the rail. They are 2 mm, 4 mm, 6 mm, 10 mm, 20 mm and 30 mm, respectively, all of them are at a 30-degree angle to the horizontal plane. In order to simplify the calculation, the rail piece is set to be movable and situated opposite to the actual scanning direction. Physical modules of dynamic mesh, magnetic field, solid heat transfer and multi-physics field are involved in the proposed model. The lift-off distance between yoke and rail surface is 5 mm, the ambient temperature is set to 293.15 K, the scanning speed of the rail is selected as 1 km/h, the output time (s) range is (0, 0.005, 0.85), the edge current of the spiral coil is set to 175 A and its frequency is intended to be 220 kHz.

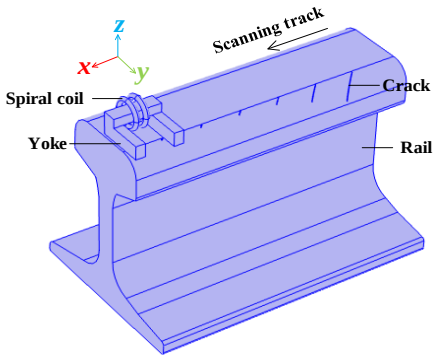

Fig. 8 Space diagram of the simulation model.

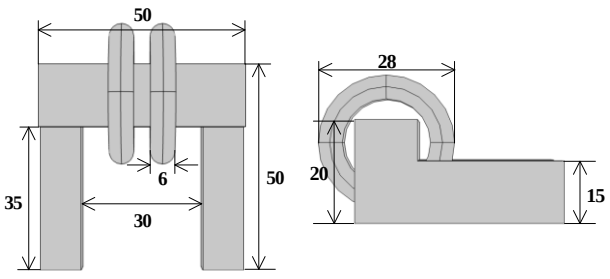

Fig. 9 (a) Top and (b) side views of the magnet yoke.

TABLE I
RELEVANT PHYSICAL PARAMETERS

Parameters \ Materials	Air	Copper	Ferrite core	Ferromagnetism steel
Conductivity (S/m)	1	5.99e7	1e-12	5.5e6
Relative dielectric constant	1	1	1	1
Relative permeability	1	1	5000	190
Heat conductivity coefficient (W/(m·K))	2.593e-2	400	5	51.9
Heat capacity (J/(kg·K))	1013	385	600	475
Density (kg/m^3)	1.205	8960	7800	7850

1) Electromagnetic Field Distribution During Inspection: The distribution of electric and magnetic fields based on numerical simulation is shown in Fig. 10. Specifically, the blue arrows denote the electric field line and the red arrows denote the magnetic field line, they are perpendicular to each other and distributed relative uniform between two yoke arms of the proposed sensing structure. This design is beneficial to enhance the sensitivity and detectability of the interesting region.

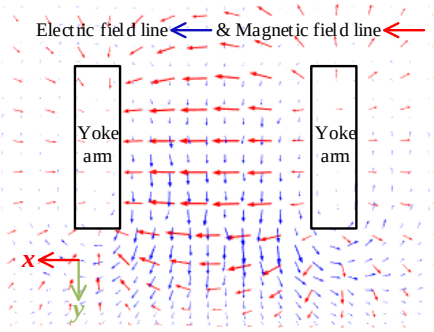

Fig. 10 Electronic field line and magnetic field line (Top view).

Since magnetic and electric fields are accompanied by each other. The magnetic flux density can be used as an indicator to express the distribution of the magnetic field. As shown in Fig. 11, the value will behave abnormally while the sensing structure moves above the cracks. In addition, it can be acquired by sensors or coils and output in the form of voltages. This is the main basis for crack detection in eddy current field. It should be noted that four cracks (crack 1, crack 2, crack 4 and crack 6) are presented and marked by red boxes successively. As can be seen from the simulation results, the values at tips or edges are significantly higher than the others, the maximum number exceed 100 mT at 0.5 s in the results of crack 4. Furthermore, each crack is revealed at the time of the excitation structure move above it, namely, each of them is located in the ROI area. Analogously, the distribution of electric fields on the surface of the rail should be studied. As shown in Fig. 12, it is apparent that the electric field around the crack in the ROI area is strong and conveniently identified, and the average values in these abnormal areas are more than 20 V/m.

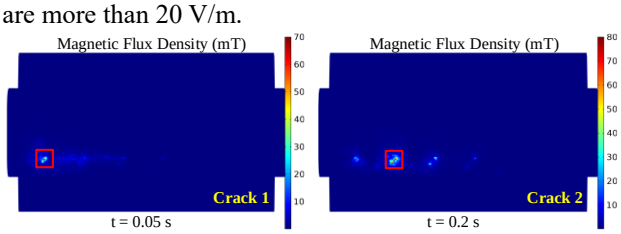

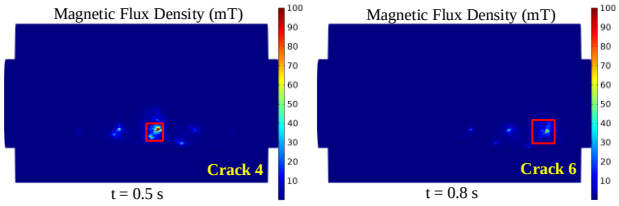

Fig. 11 Magnetic flux density (Top view).

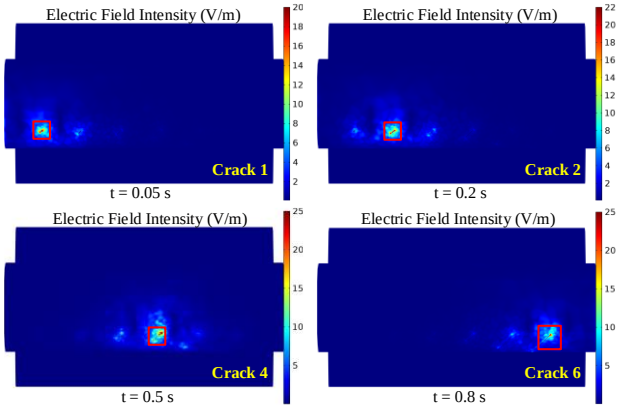

Fig. 12 Electric field intensity (Top view).

2) Thermal Field Distribution During Inspection: As elaborated in Section II, heat will be generated while there exist currents, and the thermal field can be regarded as a high-resolution reference due to the performance of the IR camera. Fig. 13 shows the distribution of the thermal field near selected four cracks during the inspection process. It is found from the simulation results that the temperature rise is not high even at a relatively low-speed condition. However, the thermal contrast is strong and benefitted the system to obtain geometric information about cracks. In addition, unlike the transient electromagnetic fields, heat will remain for a longer time due to the thermal diffusivity. The temperature rises of these cracks are visible, and in which certain of them are exceed 1.2℃ even under the speed effect.

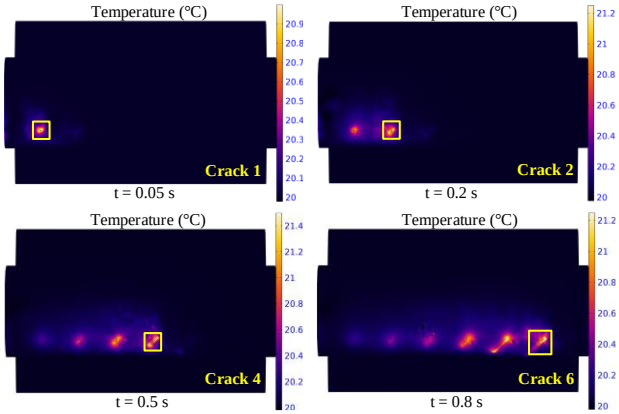

Fig. 13 Temperature (Top view).

The implementation of the above numerical simulations demonstrated the correctness of the theoretical analysis and the feasibility of the actual experiments. Consequently, it is essential to ensure the reliability of this system.

B. *Experimental Validation*

After preparation, experiments are executed to validate the effectiveness of the proposed system. The integrated system as presented in Fig. 14 contains the mentioned sensing structure, a Magnity Electronics MAG62 infrared camera, an NI USB-6366 DAQ card, a laptop with upper computer software, a custom-made carrier, a self-designed

excitation source with its synchronous controller, a water-cooling device as well as several mechanical and electrical connectors. More specifically, the wavelength band of this IR camera is 7.5-14 μm and its temperature sensitivity is lower than 60 mK when the resolution is 640×480 array with a 50 Hz frame rate. The maximum analog sampling rate of this DAQ card is 2 MHz with 8 channels. Meanwhile, the sensing structure and IR camera are fixed by a dovetail slot structure, and the former is connecting to the excitation source by adopting a 500 mm conductive hose.

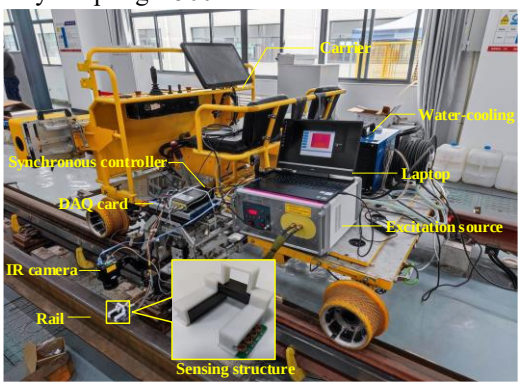

Fig. 14 Diagnostic system.

1) Details of the Specimen: In order to verify the proposed method as comprehensively as possible, a test rail which is machined by grooving and wire cut electrical discharge machining (WEDM) with 6 types of cracks is carried out. The total length of this rail is 6.25 m and it is welded together by two 60 kg/m rails with the length of 3.125 m, respectively. In addition, the main ingredient of the rail is high manganese steel and the reflection of this material is much lower than those of stainless steel that no special treatment is required for the IR camera or the rail surface in the experiments. The cracks can be categorized as different lengths, depths, burial depths, and angles, to be precise, they are 6 with different lengths (group I), 8 with different depths (group II), 6 with different burial depths (group III), 5 with different angles to the direction of track (group IV), 6 with different angles to the direction of horizontal plane (group V), as well as 8 with different depths by WEDM (group VI). The particulars of these cracks are shown in Fig. 15, it should be noted that only the cracks of group I and group V are presented, and their locations are marked with red dotted boxes. Simultaneously, all of these cracks are numbered neatly and their geometrical parameters are listed in Table II. However, the overwhelming majority of them are rolled to be closed that makes it hard to be recognized directly. Two typical examples are shown in Fig. 16.

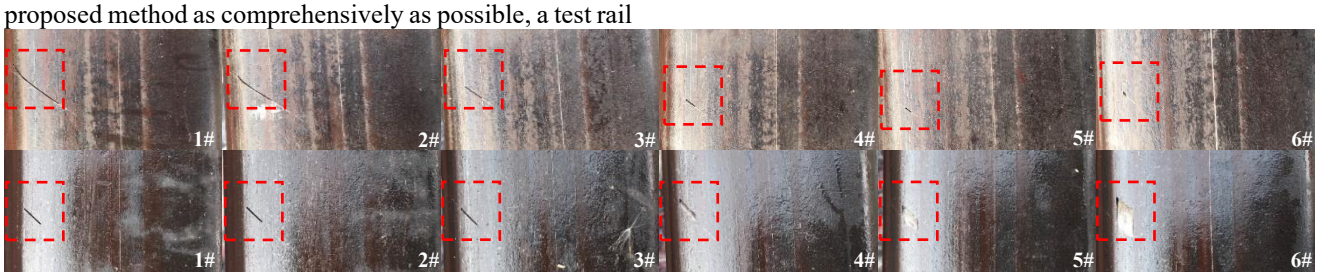

Fig. 15 On-site photos of the cracks (Rows 1-2 correspond to groups I and V, respectively).

TABLE II
DIMENSIONS OF THE CRACKS

Groups / Parameters	I (Different lengths)							II (Different depths)							
	1#	2#	3#	4#	5#	6#		1#	2#	3#	4#	5#	6#	7#	8#
Lengths(mm)	15	10	5	3	2	1	Depths(mm)	5	3.5	2.7	2	1.5	1	0.5	0.35
Depths(mm)	2.7						Lengths(mm)	5							
Angles(deg)	30						Angles(deg)	30							
	III (Different burial depths)							IV (Different angles to the direction of track)							
	1#	2#	3#	4#	5#	6#		1#	2#	3#	4#	5#			
Buried depths(mm)	7	5	3	2	1	0	Angles(deg)	90	60	45	30	15			
Lengths(mm)	5						Lengths(mm)	5							
Angles(deg)	90						Depths(mm)	2.7							
	V (Different angles to the horizontal plane)							VI (Different depths by WEDM)							
	1#	2#	3#	4#	5#	6#		1#	2#	3#	4#	5#	6#	7#	8#
Angles(deg)	90	45	30	15	10	5	Depths(mm)	5	3.5	2.7	2	1.5	1	0.5	0.35
Lengths(mm)	5						Lengths(mm)	54	46	40	35	30	25	18	16
Depths(mm)	2.7						Angles(deg)	30							


Fig. 16 Closed cracks (After rolling).

2) Experimental Set-up: On-site parameters are set as follows: *a)* The speed of the carrier is intended to be 1 km/h. *b)* The excitation current and frequency are matched to be 175 A and 220 kHz, respectively. *c)* The lift-off distance between sensing structure and rail surface is about 5 mm. *d)* The analog sampling rate of the DAQ card is 600 kHz with 4 analog channels, the resolution and frame rate of the IR camera are 640×480 array and 50 Hz, severally. It is worth mentioning that the upper machine software and synchronous controller are communicating through the serial port and they can determine the working time and sequence of the excitation source and IR camera. In this experiment, 23 s is selected as the total excitation time and the recording time is 2.2 s longer than it.

For comparison, two relatively related combined methods [21][26] are added. Ref [21] presents two separate

systems (dynamic MFL testing system and static electromagnetic thermography system) to detect and visualize the multiple cracks of the rail surface independently. The essential difference with the contrast method is that our system does not simply combine ET and ECT techniques but has the ability to physically directly coupling electromagnetic and thermal field due to the innovative design of the inverted L-type sensing structure. ET and ECT can complement each other by taking advantage of the similar excitation principles of them. Thus, electromagnetic and thermal information can be captured simultaneously by simply adopting one excitation and the inspection is wholly implemented under dynamic conditions, which will significantly enhance the detection efficiency while compared with Ref [21] in terms of the methods. Ref [26] proposes a combined NDT method based on alternating current field measurement (ACFM) and eddy current thermography technologies. A U-type magnet yoke is used in the combined system and the viewing field of IR camera does not contain the ROI between two yoke poles. A fatal problem with this design is that the IR camera cannot capture the thermal information during but only after the excitation period, which will result in the absence of partial pivotal thermal information. An extra rail piece with rolling contact fatigue (RCF) has been carried out to validate the advantages of our configuration (**See the supplementary materials for more details**). Furthermore, even if the viewing field of IR camera is adjusted to tracking the ROI, it is still difficult to be used for observing the surface of a specimen from the perpendicular direction due to the block of the beam. Instead, the proposed inverted L-type magnet yoke can get the utmost out of Lambert's cosine law and solve this problem effectively. Moreover, to further increase the credibility and highlight the advantages of the proposed method, the comparative studies of VT [10], MFL testing [21] and another double turn elliptic coil under the same conditions are also carried out. The contrasts among VT, MFL, elliptic coil and the proposed sensing structure are shown in Fig. 17. The frame rate and resolution of the VT industrial camera are 50 Hz and 640×480, the MFL probe contains a TMR sensor with vertical orientated and the lift-off is around 5 mm, the excitation frequency and amplitude are 1 kHz and ±10 V. The focal length and focal radius sum of the elliptic coil are 60 mm and 75 mm, respectively. It should be illustrated that the excitation parameters of MFL cannot be set too large due to the thin winding coils and limited measurement range of the TMR sensor. Hence, a frequently-used range (Several to dozens of V, 0.1-15 kHz) of excitation parameters in MFL or ACFM field is adopted [27].

3) Results Presentation and Analysis: Results can be obtained under the above experimental configuration. For brevity, several representative results are presented. In Fig. 18-Fig. 23, the 1st column (a) is the initial specimens, the 2nd column (b) is the results of VT and it also can be considered as on-site photos of the cracks, the 3rd-5th ((c)-(e)) columns are the results of MFL, elliptic coil and the proposed structure, respectively. The 6th column (f) is the results after anomaly detection method, which model the background of the rail datasets and consider that the patterns do not comply with the model as anomalies. The last column (g) is the energy curves which are extracted and calculated from coils array voltages. It should be noted that the relatively low contrast results in VT or elliptic coil are outlined through the orange boxes and the red marked parts in energy curves denote the corresponding cracks in ROI.

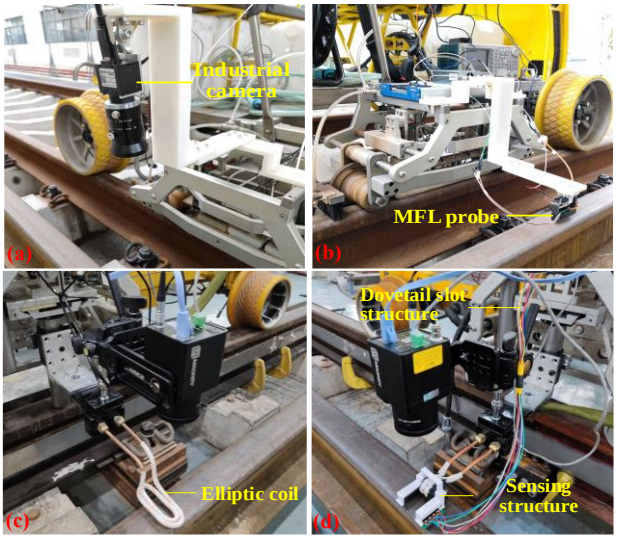

Fig. 17 Contrasts of (a) VT, (b) MFL, (c) elliptic coil and (d) the proposed structure.

a) Detection results of group I: The detection results of different lengths are satisfactory in thermography benefited to its high spatial resolution and sensitivity thus all 6 cracks can be identified. The temperature rise of the crack tips with the length over 10 mm are exceed 1.0℃ which is consistent with the results in numerical experiment. Regrettably, in this case, coils array signals will fail while the length of the crack is less than 2 mm blame to the large physical dimensions of these coils. Fig. 18 shows the comparison detection results of different crack lengths among VT, MFL, elliptic coil and the proposed structure. In particular, the crack lengths of 15 mm (1#) and 1 mm (6#) are selected to be displayed. As can be seen in Fig. 18(b), these closed cracks are difficult to distinguish directly by using VT, and from Fig. 18(c)-(d) the results by using MFL or elliptic coil are blurry and the 1 mm crack could not be detected. Fig. 18(e) and (f) show the original and after abnormal detection processing results of the proposed sensing structure, respectively. The results show a significant improvement and the outlines of these cracks in ROI are clear especially after processing. Meanwhile, the sensing structure captures the eddy current signals and supplement the results of thermograms, as shown in Fig. 18(g), the cracks in energy curves of ET are corresponding to that in thermal ones. The energy curves are exactly computed from the envelope voltage of the coil signals which is defined as:

$$e = \sum_{t=s}^{s+L} A_t^2 - (\sum_{t=s}^{s+L} A_t)^2 \tag{22}$$

where s represents current time, L denotes the time span and A_t is the amplitude of the coil envelope voltage. The fluctuations of the energy curves indicate that anomaly has been detected (defects or otherwise) in ROI, that says the result of crack 6# has been a significant underperformer.

b) Detection results of group II and VI: The experimental results of the crack with the depth of 0.35 mm are shown in Fig. 19. In comparison, the crack thermal contrast in Fig. 19(e) is higher than in Fig. 19(d) and has been significantly enhanced in Fig. 19(f). More persuasively, Fig. 20 shows

the detection results of different depths by WEDM, the depth of 0.5 mm is displayed. As can be seen in Fig. 20(d), (e) and (f), the results illustrate that the crack can be detected with high thermal contrast in thermograms, as well as, high-performance fluctuations in Fig. 20(g). Differentially, neither VT nor MFL could find the 0.35 mm depth crack (Fig. 19(b)-(c)) whereas they are applicable to the WEDM crack (Fig. 20(b)-(c)).

c) Detection results of group IV and V: Angles do not impact much effect on the detection results particularly in ferromagnetic materials due to the combined action of eddy current heat and magnetic hysteresis loss heat. Thus, the crack detection results of different angles to the direction of track have similarities in performance. Fig. 21 shows the detection results at the angle of 15° from the track direction. As the results shown in Fig. 21(e) and (f), the presence of the crack in ROI is rendered more clearly than in Fig. 21(d), this demonstrates the effectiveness of the proposed sensing structure in dynamic rail near-surface crack inspection. Fig. 22 shows the experimental results at the angle of 30° from the horizontal plane. Differently, the trailing effect of heat seems obvious due to the small angle from the plane, and it will increase as the angle decreases.

d) Challenging study (Detection results of group III): The buried crack detection is considered as a challenging study of electromagnetic thermography. It is difficult to detect buried defects in metal materials with pure ECT technology unless the depth is especially shallow, and this phenomenon will be aggravated in ferromagnetic materials with high magnetic permeability. It can be seen from Fig. 23(a), the crack is machined from the side view and it is 1 mm away from the rail surface. Neither the elliptic coil nor the inverted L-type magnet yoke can detect this crack successfully (as shown in Fig. 23(d)-(f)), hence the signal compensation of the coils array is necessary. Fig. 23(g) indicates the appearance of the buried crack will disturb the coil signals and arouse voltage fluctuation, which can be used to determine whether there are subsurface defects that ECT cannot detect intuitively. Nonetheless, the detection results would be unsatisfactory while the defect is buried too deep. For instance, in these experiments, defects with the buried depths greater than 2 mm cannot be detected.

In the quantitative aspect, the signal-to-noise ratio (SNR) is generally adopted to evaluate the detectability of a system or a method. The expression of SNR (PSNR) can be defined as [28]:

$$\mathrm{SNR(PSNR)} = 20\lg(\frac{T_D}{T_N})[\mathrm{dB}] \tag{23}$$

where T_D denotes the average temperature or maximum energy value in defective area and T_N denotes the average temperature or fiducial energy value in non-defective area. Whereas in the thermal detection, the thermal contrast (TC) is generally used to quantify the sensitivity. The expression can be defined as follows:

$$\mathrm{TC} = \frac{T_D - T_N}{T_N - T_0} \tag{24}$$

where TC denotes the thermal contrast and T_0 denotes the ambient temperature. The quantized values of TC, SNR and PSNR are listed in Table III, it should be noted that TC and SNR represents the quantization of thermal images while PSNR represents the quantization of MFL or eddy current signals. In this table, the symbol of "--" refers to the omission of this way. Besides, the detectable rate of VT, MFL, elliptic coil and the coupled sensing structure are computed, which are 7/39 ≈ 17.9%, 28/39 ≈ 71.8%, 30/39 ≈ 76.9% and 36/39 ≈ 92.3%, separately.

Conclusively, from the detection results, VT produces insufficient effect on closed cracks and the defects can be observed only when they exhibit obvious opening property. MFL is insensitivity to the slightly smaller cracks and it is difficult to identify the morphology. Although elliptic coil and the proposed method have the ability to detect the vast majority of the cracks, the detection quality of the proposed system is much better than the former. More importantly, the buried defects are completely undetectable while adopting the elliptic coil (Fig. 23(d)) whereas the proposed method has effectively mitigated this problem (Fig. 23(g)). This is not just an increase in metrics, but an expansion of the categories of detectable defects, which is a meaningful work in the field of structural fault diagnosis.

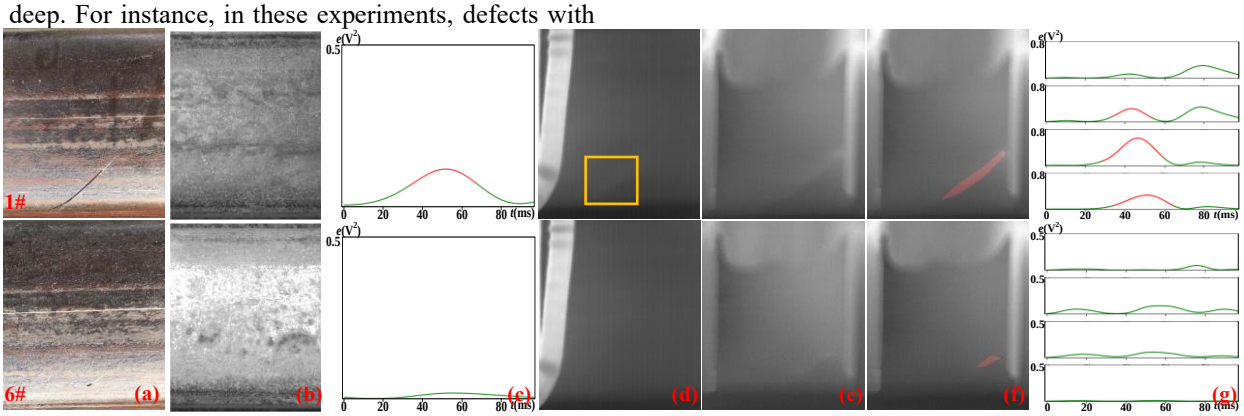

Fig. 18 Experimental results of group I. (a) Crack 1# and 6#. (b) VT. (c) MFL (normalization). (d) Elliptic coil. (e) The proposed structure (original). (f) After anomaly detection method. (g) Energy curves (normalization).

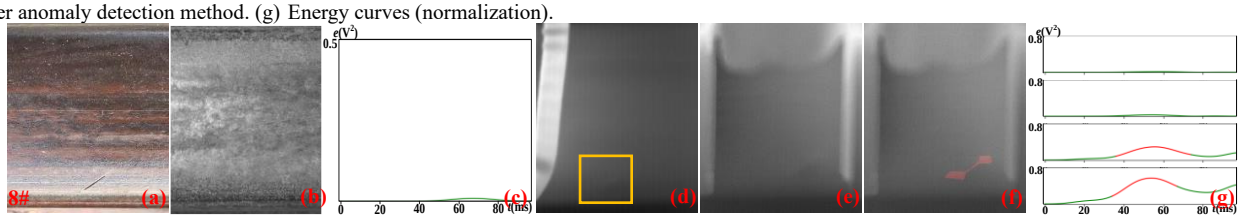

Fig. 19 Experimental results of group II. (a) Crack 8#. (b) VT. (c) MFL (normalization). (d) Elliptic coil. (e) The proposed structure (original). (f) After anomaly detection method. (g) Energy curves (normalization).

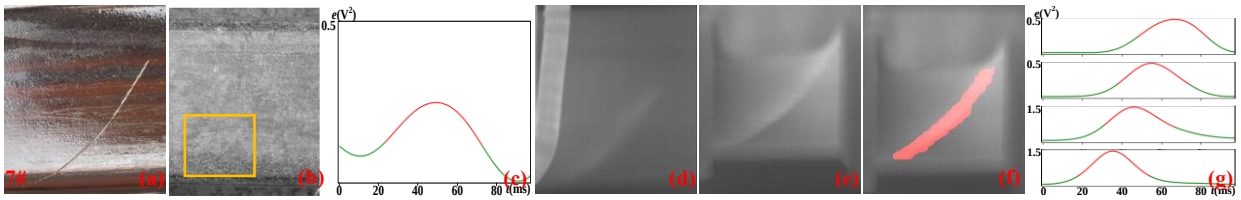

Fig. 20 Experimental results of group VI. (a) Crack 7#. (b) VT. (c) MFL (normalization). (d) Elliptic coil. (e) The proposed structure (original). (f) After anomaly detection method. (g) Energy curves (normalization).

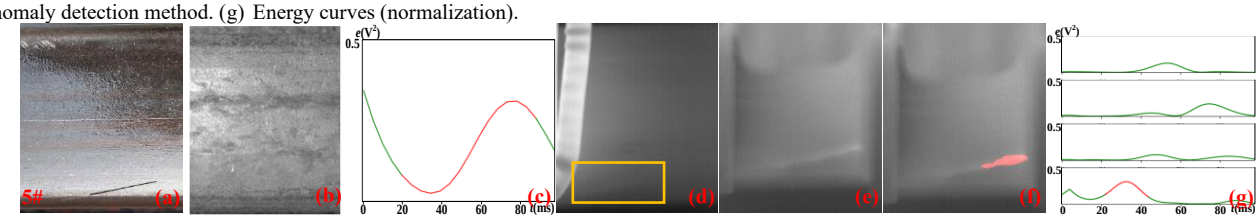

Fig. 21 Experimental results of group IV. (a) Crack 5#. (b) VT. (c) MFL (normalization). (d) Elliptic coil. (e) The proposed structure (original). (f) After anomaly detection method. (g) Energy curves (normalization).

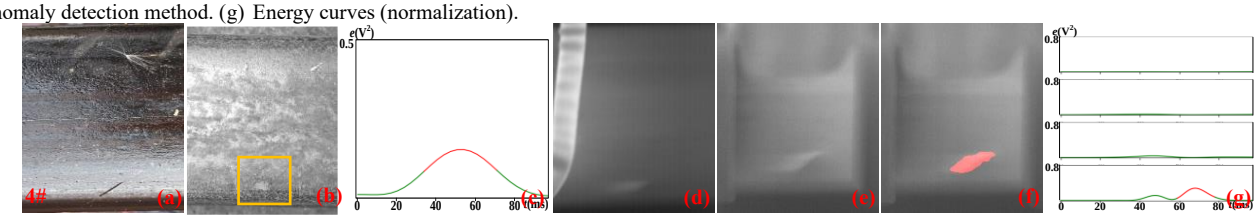

Fig. 22 Experimental results of group V. (a) Crack 3#. (b) VT. (c) MFL (normalization). (d) Elliptic coil. (e) The proposed structure (original). (f) After anomaly detection method. (g) Energy curves (normalization).

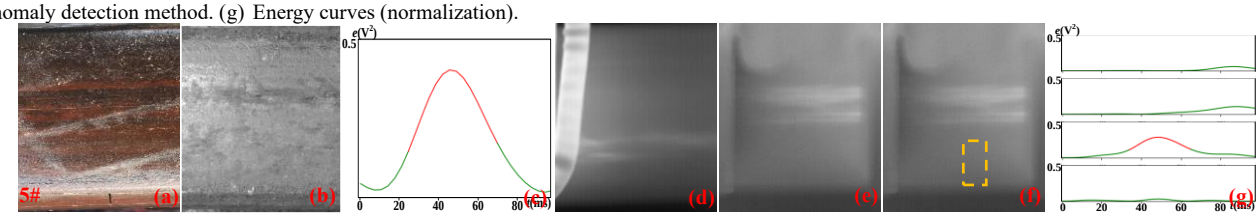

Fig. 23 Experimental results of group III. (a) Crack 5#. (b) VT. (c) MFL (normalization). (d) Elliptic coil. (e) The proposed structure (original). (f) After anomaly detection method. (g) Energy curves (normalization).

TABLE III

TC, SNR, PSNR AND DETECTABLE RATE OF CRACK DETECTION EXPERIMENTS

		Group I 1#	Group I 6#	Group II 8#	Group VI 7#	Group IV 5#	Group V 3#	Group III 5#
TC	elliptic coil	0.823	--	0.229	1.125	0.585	0.778	--
	proposed	2.481	0.974	2.174	3.233	1.825	2.833	--
SNR	elliptic coil	0.881	--	0.457	2.110	0.636	1.548	--
	proposed	4.815	3.052	3.659	5.460	4.814	4.940	--
PSNR	MFL	5.634	--	--	2.315	5.346	5.905	5.701
	proposed	4.776	--	3.311	5.298	9.940	6.088	9.056
Detectable Rate	VT		17.9%		MFL		71.8%	
	elliptic coil		76.9%		**proposed**		92.3%	

Ulteriorly, the schematic diagram of defects distribution on the rail near-surface is shown in Fig. 24, the total length of the rail specimen is 6.25 m, I-VI represent the defects group I-VI and their adjacent spacing distances are 300 mm where the distances between their internal defects are 100 mm. Thus, as shown in Fig. 24, the regional patches subdivision of the rail surface is carried out and the width of these blue patches are 100 mm except for which immediately adjacent to the weld joint. In this context, the rail surface can be divided into 63 parts and the confusion matrix to evaluate the effect can be obtained by statistical analysis of the detection situation of these regional patches. In these patches, assuming that the true positive (TP) denotes the defective ones which are successfully detected, false negative (FN) denotes the defective ones which are not detected, false positive (FP) denotes the non-defective ones which are false alarmed and true negative (TN) denotes the non-defective ones which are not alarmed. Hereby, the confusion matrix about detection results of the proposed system can be presented in Fig. 25. It can be seen that 36 of the 39 defects have been successfully detected, 3 buried defects with profound depths are missed and 5 non-defective patches are false alarmed due to the potential impurities of rail or jitter of the sensing structure.

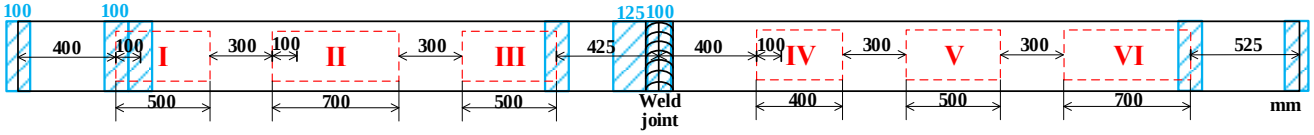

Fig. 24 Schematic diagram of defects distribution on the rail near-surface (Top view).

		Practical	
		Positive	Negative
Detective	Positive	36 TP	5 FP
	Negative	3 FN	19 TN

Fig. 25 Confusion matrix.

IV. Discussion

Based on the current situation, two limitations are identified with the proposed method:

1) The speed of dynamic scanning cannot be too fast due to the limitations of acquisition equipment (IR camera) and mechanical platform. That is, the response time of camera limits the thermal image acquisition in high speed motion mode that results in blurring of images. In addition, the speed will affect the per unit time of excitation transmission energy which would further weaken the detection effect of induction thermography.

2) The depth quantification of defect is difficult. Depth quantification has always been a challenge in the industrial field of NDT due to the potential jitter of the sensing structure during the inspection process. For addressing this challenge, our preliminary relevant studies are already under way [29]. For instance, in terms of group VI, the method of skewness (**See the supplementary materials for more details**) has been considered to evaluate their depths and has obtained the certain effect. Nevertheless, it is a preliminary calculation under laboratory conditions and still far from being applied to industrial site due to the rough accuracy in the case of dynamic inspection as well as the relatively limited variety of quantifiable defects.

V. Conclusion and Future Work

In this paper, a feasible dynamic rail inspection of a multi-physical coupled electromagnetic and thermography sensing system is proposed. The theoretical model of the coupling field is derived. The simulation and experimental results of the rail sample are investigated. Several conclusions can be summarized:

1) The proposed integrated prototype is competent for detecting the rail cracks of multiple categories at the speed of 1 km/h and has the ability to mark defects automatically with the aid of abnormal learning strategy. It lays the foundation for long-distance automated railway safety inspections which is urgently required in the field of railway diagnosis industrial application.

2) The multi-physical coupled sensing structure is demonstrated to conspicuously enhance the sensitivity and detectability of the inspection system compared with the conventional methods of VT, MFL and elliptic coil.

3) The experimental results verify the defects with burial depths which is less than 2 mm can be detected with the critical supplement of the coils array and it is a great difficulty in pure ECT technology in motion.

Future works will concentrate on optimizing the sensing structure as well as the crack depths quantification method at an increasing inspection speed.

VI. Acknowledgement

The work was supported by National Natural Science Foundation of China (No. 61971093, No. 61527803, No. 61960206010). The work was supported by Science and Technology Department of Sichuan, China (Grant No.2019YJ0208, Grant No.2018JY0655, Grant No. 2018GZ0047) and Fundamental Research Funds for the Central Universities (Grant No. ZYGX2019J067).

References

[1] M. Ph. Papaelias *et al*., "A review on non-destructive evaluation of rails: state-of-the-art and future development," *Proceedings of the Institution of Mechanical Engineers Part F Journal of Rail & Rapid Transit*., vol. 222, no. 4, pp. 367-384, 2008.

[2] S. L. Grassie, "Rolling contact fatigue on the British railway system: treatment," *Wear*, vol. 258, no. 7, pp. 1310-1318, 2005.

[3] H. Lei and G. Tian, "Broken wire detection in coated steel belts using the magnetic flux leakage method," *Insight, Non-Destructive Testing and Condition Monitoring*., vol. 55, no. 3, pp. 126-131, 2013.

[4] A. G. Antipov *et al*., "Evaluation of transverse cracks detection depth in MFL rail NDT," *Russian Journal of Nondestructive Testing*., vol. 50, no. 8, pp. 481-490, 2014.

[5] S. Huang *et al*., "An opening profile recognition method for magnetic flux leakage signals of defect," *IEEE Trans. Instrum. Meas*, vol. 68, no. 6, pp. 2229-2236, 2019.

[6] R. S. Edwards *et al*., "Characterisation of defects in the railhead using ultrasonic surface waves," *NDT & E Int*., vol. 39, No. 6, pp. 468-475, 2006.

[7] G. P. P. Gunarathne and Y. Qureshi, "Development of a synthetic a-scan technique for ultrasonic testing of pipelines," *IEEE Trans. Instrum. Meas.*, vol. 54, no. 1, pp. 192-199, 2005.

[8] S. Chen *et al*., "An acoustic-homologous transfer learning approach for acoustic emission-based rail condition evaluation," *Structural Health Monitoring*., vol. 20, no. 1, 2020, Art. no. 147592172097694.

[9] M. Yu *et al*., "Acoustic emission enabled particle size estimation via low stress-varied axial interface shearing," *IEEE Trans. Instrum. Meas.*, vol. 71, pp. 1-10, 2022.

[10] E. Resendiz *et al*., "Automated visual inspection of railroad tracks," *IEEE Trans. Intel. Transp. Sys*., vol. 14, no. 2, pp. 751-760, 2013.

[11] Q. Luo *et al*. "Automated visual defect detection for flat steel surface: a survey," *IEEE Trans. Instrum. Meas.*, vol. 69, no. 3, pp. 626-644, 2020.

[12] T. Lee, *et al*., "Analysis of the eddy current signal due to defects on a railway," *New Physics Sae Mulli*., vol. 69, no. 4, pp. 361-368, 2019.

[13] X. Chen *et al*., "Inversion method in pulsed eddy current testing for wall thickness of ferromagnetic pipes," *IEEE Trans. Instrum. Meas.*, vol. 69, no. 12, pp. 9766-9773, 2020.

[14] R. Yang *et al*., "Lateral heat conduction based eddy current thermography for detection of parallel cracks and rail tread oblique cracks," *Measurement*, vol. 66, pp. 54-61, 2015.

[15] X. Chen *et al*., "Tomographic reconstruction of rolling contact fatigues in rails using 3D eddy current pulsed thermography," *IEEE Sens. J*., vol. 21, no. 17, pp. 18488-18496, 2021.

[16] P. Wang *et al*., "Velocity effect analysis of dynamic magnetization in high speed magnetic flux leakage inspection," *NDT & E Int*., vol. 64, no. 6, pp. 7-12, 2014.

[17] S. Hu *et al*., "Rapid detection of cracks in the rail foot by ultrasonic B-scan imaging using a shear horizontal guided wave electromagnetic acoustic transducer," *NDT & E Int*., vol. 120, no. 2, 2021, Art. no. 102437.

[18] N. A. Thakkar *et al*., "Rail-wheel interaction monitoring using acoustic emission: a laboratory study of normal rolling signals with natural rail defects," *Mechanical Systems and Signal Processing*., vol. 24, no. 1, pp. 256-266, 2010.

[19] Z. Song, "Detection of damage and crack in railhead by using eddy current testing," *J. Electromagnetic Analysis & Applications*., vol. 3, no. 12, pp. 546-550, 2012.

[20] H. Li *et al*., "Multiphysics structured eddy current and thermography defects diagnostics system in moving mode," *IEEE Trans. Ind. Informat*., vol. 17, no. 4, pp. 2566-2578, 2021.

[21] Y. Gao *et al*., "Multiple cracks detection and visualization using magnetic flux leakage and eddy current pulsed thermography," *Sens. Actuators A. Phys*., vol. 234, pp. 269-281, 2015.

[22] F. Yuan *et al*., "Investigation of DC electromagnetic-based motion induced eddy current on NDT for crack detection," *IEEE Sens. J*., vol. 21, no. 6, pp. 7449-7457, 2021.

[23] Z. Hou, “Solid heat conduction,” *Shanghai Scientific & Technical Publishers*, vol. 4, pp. 73-94, 1984.
[24] M. Bicego and M. Figueiredo, “Soft clustering using weighted one-class support vector machines,” *Pattern Recognition*, vol. 42, no. 1, pp. 27-32, 2009.
[25] X. Zhang *et al*., “Memory linked anomaly metric learning of thermography rail defects detection system,” *IEEE Sens. J.*, vol. 21, no. 21, pp. 24720-24730, 2021.
[26] M He *et al*., “Study on a combined NDT method based on ACFM and eddy current thermography,” *Nondestructive Testing and Evaluation*., vol. 34, no. 2, pp. 147-163, 2019.
[27] W Li *et al*. “Analysis of the inducing frequency of a U-shaped ACFM system,” *NDT & E Int*., vol. 44, pp. 324-328, 2011.
[28] Z. Liu *et al*., “Natural crack diagnosis system based on novel l-shaped electromagnetic sensing thermography,” *IEEE Trans. Ind. Electron*., vol. 67, no. 11, pp. 9703-9714, 2020.
[29] Y Liu *et al*., “Depth quantification of rolling contact fatigue crack using skewness of eddy current pulsed thermography in stationary and scanning modes,” *NDT & E Int*., vol. 128, 2022, Art. no. 102630.